Volume 23
Number 18
14 May 2021
Pages 3241–3420

CrystEngComm

rsc.li/crystengcomm

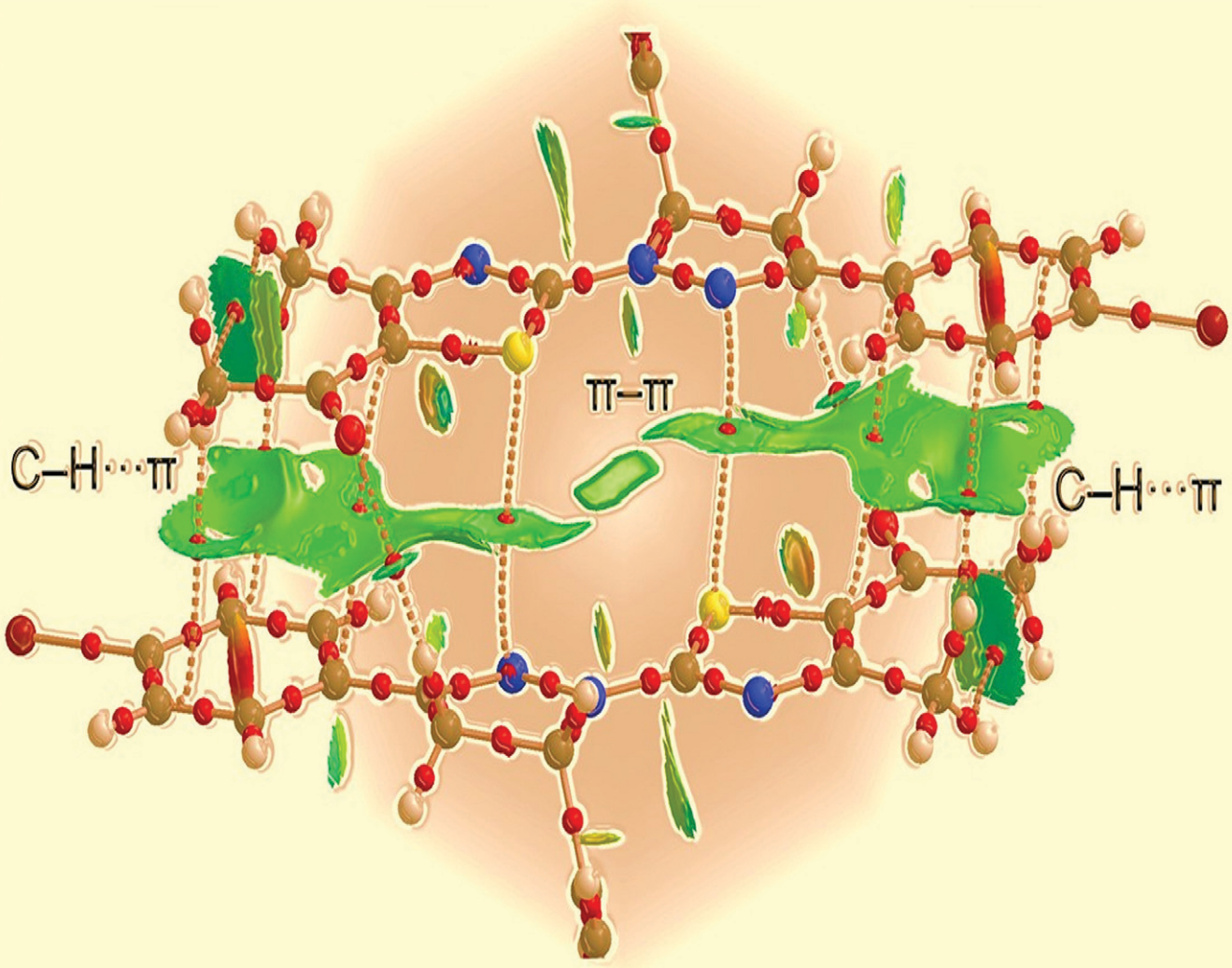

ISSN 1466-8033

ROYAL SOCIETY OF CHEMISTRY

PAPER
Muhammad Naeem Ahmed, Murtaza Madni, Antonio Frontera *et al.*
Crystal engineering with pyrazolyl-thiazole derivatives: structure-directing role of π-stacking and σ-hole interactions

CrystEngComm

ROYAL SOCIETY OF CHEMISTRY

PAPER

View Article Online
View Journal | View Issue

Cite this: *CrystEngComm*, 2021, **23**, 3276

Crystal engineering with pyrazolyl-thiazole derivatives: structure-directing role of π-stacking and σ-hole interactions†

Muhammad Naeem Ahmed, *[a] Murtaza Madni,*[b] Shaista Anjum,[a] Saiqa Andleeb,[c] Shahid Hameed, [b] Abdul Majeed Khan,[d] Muhammad Ashfaq,[e] Muhammad Nawaz Tahir,[e] Diego M. Gil [f] and Antonio Frontera *[g]

Received 22nd February 2021,
Accepted 9th March 2021

DOI: 10.1039/d1ce00256b

rsc.li/crystengcomm

The synthesis and X-ray characterization of 1-(2-(3-(4-bromophenyl)-5-(4-methoxyphenyl)-4,5-dihydro-1*H*-pyrazol-1-yl)-4-methylthiazol-5-yl)ethanone (**7**), ethyl 2-(5-(4-bromophenyl)-3-(4-chlorophenyl)-4,5-dihydropyrazol-1-yl)thiazole-4-carboxylate (**8**) and 2-(5-(4-chlorophenyl)-3-phenyl-4,5-dihydro-1*H*-pyrazol-1-yl)-*N*′-(2-hydroxy-3-methoxybenzylidene)thiazole-4-carbohydrazide (**10**) are described in this manuscript. The structure-directing role of a variety of noncovalent interactions has been analyzed energetically using DFT calculations and Hirshfeld surface analysis. Moreover, the existence and importance of halogen and chalcogen bonding interactions have been analyzed by using the quantum theory of atoms in molecules and the noncovalent interaction index (NCIplot).

Introduction

Compounds with pyrazole moieties play an important role in active pharmaceutical drugs and agrochemicals in controlling infections, diseases and pests.[1–3] Several drugs have been developed in recent years from pyrazole derivatives. For example, celecoxib demonstrates anti-inflammatory effects and inhibits COX-2; rimonabant functions as a cannabinoid receptor and is also used to treat obesity.[4] Moreover, pyrazole derivatives have shown significant biological activities such as antimicrobial, analgesic, anti-inflammatory, and anticancer activities.[5–7] The significance of thiazoles is emphasized because they are precursors for the synthesis of several drugs, such as ravuconazole,[8] an antifungal agent, and nizatidine,[9] an antiulcer agent (Scheme 1). In addition, the thiazole group is also important in drug designing, since it frequently appears in the structures of various natural products and biologically active compounds like thiamine and in some antibiotic drugs like penicillin, micrococcin and many metabolic products of fungi and primitive marine animals.

In addition, combined pyrazolyl-thiazole scaffolds are also relevant for several medical and pharmaceutical applications. Their derivatives are potent antiviral[10] and anti-inflammatory[11]

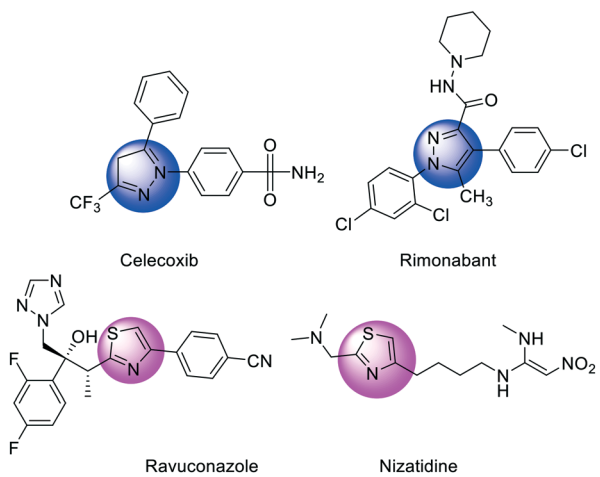

Scheme 1 Structure of celecoxib, rimonabant, ravuconazole and nizatidine.

[a] *Department of Chemistry, The University of Azad Jammu and Kashmir, Muzaffarabad, 13100 Pakistan*
[b] *Department of Chemistry, Quaid-i-Azam University, Islamabad 45320, Pakistan*
[c] *Department of Zoology, The University of Azad Jammu and Kashmir, Muzaffarabad, 13100 Pakistan*
[d] *Research Laboratory of Bioenergy, Department of Chemistry, Federal Urdu University of Arts, Science and Technology, Gulshan-e-Iqbal Campus, University Road, Karachi-75300, Pakistan*
[e] *Department of Physics, University of Sargodha, Sargodha, Pakistan*
[f] *INBIOFAL (CONICET – UNT), Instituto de Química Orgánica, Facultad de Bioquímica, Química y Farmacia, Universidad Nacional de Tucumán, Ayacucho 471, T4000INI, San Miguel de Tucumán, Argentina. E-mail: diego.gil@fbqf.unt.edu.ar*
[g] *Department of Quimica, Universitat de les Illes Balears, Crta. De Valldemossa Km 7.5, 07122 Palma de Mallorca, Baleares, Spain*

† Electronic supplementary information (ESI) available: Hirshfeld surfaces of compounds **7**, **8** and **10** mapped over shape index and curvedness properties (Fig. S1). CCDC 1981404, 1009301 and 1009302. For ESI and crystallographic data in CIF or other electronic format see DOI: 10.1039/d1ce00256b

agents, AChE inhibitors,[12] antimicrobiotics[13] and EP1 receptor antagonists.[14,15] Motivated by the aforementioned findings and pursuing our studies on different five-membered heterocycles[16–19] as well as structural studies,[20] we have designed new derivatives with pyrazolyl-thiazole moieties (Scheme 2). Similarly, in continuation of our recent studies on antiparallel π–π interactions in isatin-based hydrazides,[21] π-hole tetrel bonding in 2-triazolyl-2-oxoacetate derivatives[22] and recurrent π-stacking motifs in pyrazolyl-thiazole–coumarin hybrids,[23] we report herein synthetic protocols to access aryl-substituted pyrazolyl-thiazole derivatives. The structures reported herein exhibit interesting solid-state architectures with an intricate combination of interactions, including unconventional π-interactions where the nonaromatic pyrazolyl ring is stacked over the aromatic thiazole ring and *vice versa*. Moreover, the role of halogen and chalcogen bonding interactions is also analysed using several computational tools, including molecular electrostatic potential surfaces and a combination of quantum theory of atoms in molecules (QTAIM) and NCIplot analyses.

Experimental and theoretical methods

Instrumentation and synthesis

All reagents were commercially available and used without further purification. Melting points were determined on a Stuart SMP3 melting point apparatus and are uncorrected. IR spectra were recorded on a Thermo Scientific Nicolet 6700 FTIR spectrophotometer using ATR facility. ^{1}H and ^{13}C NMR spectra were recorded on a Bruker Avance 300 MHz instrument in deuterated solvents and the chemical shifts are referenced to TMS. Reactions were monitored using thin layer chromatography (TLC) on silica gel 60F254 coated aluminium sheets (Merck, Germany). X-ray diffractometer analysis was carried out on a Bruker Kappa APEX-IICCD diffractometer.

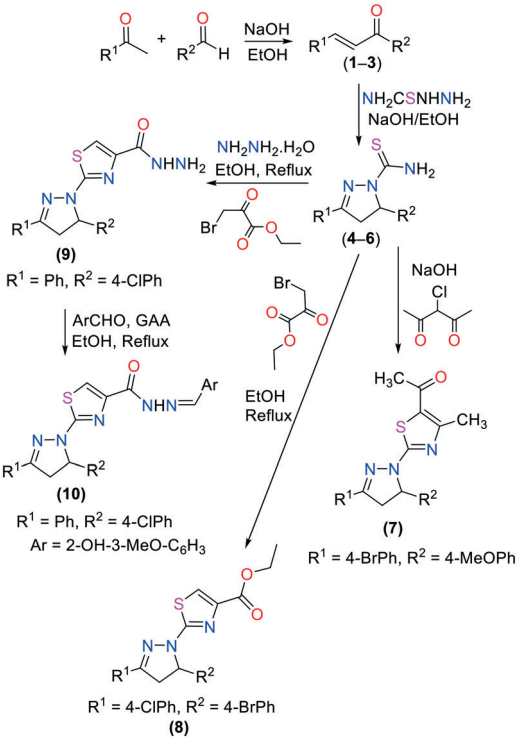

Scheme 2 Synthetic route to compounds **4–10**.

The synthetic route to compounds **4–10** is shown in Scheme 2. By following a procedure already reported in the literature[12,24–26] a mixture of substituted acetophenone (5.0 mmol) and 4-substituted benzalaldehyde (5.0 mmol) in 20 mL of ethanol (EtOH) was stirred at room temperature followed by the dropwise addition of an aqueous solution of NaOH (10 M). The stirring was continued for 2 h. After reaction completion verified by TLC, the reaction mixture was poured into ice-cold water to obtain yellow precipitates. The solid mass was filtered, washed with excess water and recrystallized from EtOH to obtain compounds **1–3**. Similarly, compounds **1–3** (1 mmol) and thiosemicarbazide (1 mmol) were dissolved in 20–25 mL of ethanol and stirred vigorously.[12,23] Pellets of NaOH (1.5 mol) were added to the reaction mixture and heated under reflux. After reaction completion (TLC), the suspension was poured into ice-cold water. The light yellow precipitates formed were filtered and recrystallized from methanol (MeOH) to give compounds **4–6**. For the synthesis of compound **7**, 2 mmol of **4** (5-dihydro-3,5-diphenylpyrazole-1-carbothioamide) and 2 mmol of 3-chloropentane-2,4-dione were loaded in 100 mL of RBF. Ethanol was used as solvent. This reaction mixture was stirred for 30 minutes at 50 °C. After completion of the reaction, the whole mixture was transferred to a beaker containing crushed ice. The resulting precipitates were filtered and washed with cold ethanol. After drying, the solid was recrystallized in EtOH : EtOAc (1 : 1) to obtain compound **7**.

Compounds **4–6** (1.00 mmol) and α-bromopyruvate (1.0 mmol) were dissolved in ethanol with vigorous stirring at 50–60 °C for 3–4 h. 2,4-Disubstituted-1,3-thiazole **8** precipitate was filtered out and the solid mass obtained was washed with ethanol and recrystallized from $CHCl_3$: EtOH (3 : 1).[10] Compound **9** (1.0 mmol) and the respective benzaldehyde (1 mmol) were added to 20 mL ethanol containing a catalytic amount of acetic acid. The reaction mixture was refluxed till completion (TLC). The mixture was poured into ice-cold water and the precipitate was filtered. The solid formed was then recrystallized from $CHCl_3$: EtOH (3 : 1)[10] to obtain **10**.

1-(2-(3-(4-Bromophenyl)-5-(4-methoxyphenyl)-4,5-dihydro-1*H*-pyrazol-1-yl)-4-methylthiazol-5-yl)ethanone (7). Molecular formula: $C_{22}H_{20}BrN_3O_2S$, Mol. wt. = 470.382, yellow solid, m. p. = 144–146 °C, yield = 82%, R_f = 0.45; IR ($\bar{\nu}$, ATR, cm^{-1}): 3122 (Ar–H), 2927 (C–H), 1618 (C=O), ^{1}H NMR (300 MHz, $CDCl_3$) = δ ppm 2.45 (3H, s, CH_3), 2.53 (s, 3H, CH_3), 3.3 (dd, 1H, J_{cis} = 7.2 Hz, J_{gem} = 17.4 Hz), 3.8 (s, 3H, –OCH_3), 4.03 (dd, 1H, J_{trans} = 12 Hz, J_{gem} = 17.4 Hz), 5.65 (dd, 1H, J_{cis} = 7.2 Hz, J_{trans} = 12 Hz), 6.92 (m, 2ArH), 7.25, (m, 2ArH), 7.6 (m, 4ArH); ^{13}C-NMR (75 MHz, $CDCl_3$): δ ppm 18.95, 30.06, 43.46, 56.2, 60.94, 106.8, 114.1, 125.4, 128, 131.4, 131.8, 133, 135.8, 158.7, 151.8, 156.6, 167.6, 189.6.

Ethyl 2-(5-(4-bromophenyl)-3-(4-chlorophenyl)-4,5-dihydropyrazol-1-yl)thiazole-4-carboxylate (8). Molecular formula: $C_{21}H_{17}BrClN_3O_2S$, Mol. wt. = 490.80, yellow solid, m. p. = 149–151 °C, yield = 75%, R_f = 0.51; IR ($\bar{\nu}$, ATR, cm^{-1}): 3033 (C═C–H), 2985 (C–H), 1698 (C═O), ^{1}H NMR (300 MHz, $CDCl_3$): δ = 1.34 (t, 3H, J = 7.2 Hz), 3.32 (dd, 1H, J_{cis} = 5.4 Hz, J_{gem} = 17.4 Hz), 3.90 (dd, 1H, J_{trans} = 12.0 Hz, J_{gem} = 17.7 Hz), 4.30 (m, 2H), 5.73 (dd, 1H, J_{cis} = 5.7 Hz, J_{trans} = 12 Hz), 7.31–7.45 (m, 6 ArH), 7.54 (s, 1H), 7.75–7.79(m, 2ArH; ^{13}C NMR (75 MHz, $CDCl_3$): δ ppm 14.1, 44.4, 61.5, 63.3, 118.9, 126.0, 127.2, 128.9, 129.1, 130.6, 131.2, 133.5, 139.6, 143.8, 152.1, 160.3, 165.8.

2-(5-(4-Chlorophenyl)-3-phenyl-4,5-dihydro-1*H*-pyrazol-1-yl)-*N*′-(2-hydroxy-3-methoxybenzylidene)thiazole-4-carbohydrazide (10). Molecular formula: $C_{27}H_{22}ClN_5O_3S$, Mol. wt. = 532.00, light yellow solid, m.p. = 220–222 °C, yield = 65%, R_f = 0.52; IR ($\bar{\nu}$, ATR, cm^{-1}): 3242 (NH), 3014 (C–H aromatic), 2926 (C–H aliphatic), 1702 (C═O amidic), 1587 (C═N), 1564 (C═C); ^{1}H NMR (300 MHz, $CDCl_3$) = δ ppm 3.44(dd, 1H, J_{cis} = 5.7 Hz, J_{gem} = 18.0 Hz), 3.81 (s, 3H, OCH_3), 3.85 (bs, 1H, OH), 4.12 (dd, 1H, J_{trans} = 11.7 Hz, J_{gem} = 18.0 Hz), 5.76 (dd, 1H, J_{cis} = 5.7 Hz, J_{trans} = 11.7 Hz), 6.85–7.51 (m, 9ArH), 7.72, (s, 1H), 7.80–7.83 (m, 3ArH), 8.67 (1, 1NH), 11.25 (1, 1H); ^{13}C NMR (75 MHz, DMSO): δ ppm 43.4, 56.3, 63.5, 114.4, 116.7, 119.4, 119.5, 121.3, 127.1, 129.1, 129.2, 129.4, 130.8, 131.0, 132.8, 140.7, 145.0, 147.6, 148.4, 154.5, 149.0, 157.3, 164.8.

Hirshfeld surface calculations

Analysis of the Hirshfeld surfaces (HS) and the corresponding two-dimensional fingerprint plots (full and decomposed)[27] was carried out employing the CrystalExplorer17.5 (ref. 28) program to visualize and quantify different intermolecular interactions. The Hirshfeld surfaces were mapped over d_{norm} shape index and curvedness properties. The d_{norm} is a symmetric function of distances to the surface from nuclei inside and outside the HS (d_i and d_e, respectively), relative to their respective van der Waals (vdW) radii, which enables identification of the regions of particular importance to intermolecular interactions. The d_{norm} surfaces were mapped over a fixed color scale of −0.050 a.u. (red) to 0.750 Å a.u. (blue). The shape index property is based on the local curvature of the surface, and it is especially useful to identify planar π-stacking arrangements.[27a]

The interaction energies were computed using a dispersion-corrected CE-B3LYP/6-31G(d,p) level of theory available in the CrystalExplorer17.5 program.[28] The total energy (E_{tot}) is the sum of four main components, including electrostatic (E_{ele}), polarization (E_{pol}), dispersion (E_{dis}), and exchange-repulsion (E_{rep}) energies, with scale factors of 1.057, 0.740, 0.871 and 0.618, respectively.[29]

Theoretical methods

The DFT calculations presented in the last section of the manuscript were carried out using the Gaussian-16 program[30] at the PBE0 (ref. 31)-D3 (ref. 32)/def2-TZVP (ref. 33) level of theory and using the crystallographic coordinates. The formation energies of the assemblies were evaluated by calculating the difference between the total energy of the assembly and the sum of the monomers that constitute the assembly, which were kept frozen. The molecular electrostatic potential was computed at the same level of theory and plotted onto the 0.001 a.u. isosurface. The QTAIM (ref. 34) distribution of critical points (CPs) and NCIplot[35,36] isosurfaces have been used to characterize noncovalent interactions. They correspond to both favourable and unfavourable interactions, as differentiated by the sign of the second density Hessian eigenvalue and defined by the isosurface colour. The colour scheme is a red-yellow-green-blue scale with red for ρ^+_{cut} (repulsive) and blue for ρ^-_{cut} (attractive).

X-ray data collection and structure refinement

Suitable single crystals grown from EtOH:EtOAc of compounds **7**, **8** and **10** were selected for X-ray analyses, and diffraction data were collected on a Bruker Kappa APEX-II CCD detector with MoK_α radiation at 296 K. Semi-empirical correction was applied using the SADABS program.[37] All the structures were solved by direct methods using the SHELX program.[38] The positions and anisotropic parameters of all non-H atoms were refined on F^2 using the full matrix least-squares technique. The H atoms were added at geometrically calculated positions and refined using the riding model. The details of crystallographic data and crystal refinement parameters for compounds **7**, **8** and **10** are given in Table 1.

Results and discussion

Description of crystal structures of compounds 7, 8 and 10

The molecular structures of compounds **7**, **8** and **10** are shown in Fig. 1. Crystal data and structure refinement are presented in Table 1. Compounds **7** and **8** crystallize in the triclinic crystal system with the centrosymmetric $P\bar{1}$ space group accommodating two molecules and one molecule per unit cell, respectively. Compound **10** crystallizes in the orthorhombic $Pca2_1$ space group with Z = 4 molecules per unit cell.

In **7**, the bromophenyl moiety A (C1–C6/Br1), 4,5-dihydro-1*H*-pyrazole ring B (C7–C9/N1/N2), anisole moiety C (C10–C16/O1) and 1-(4-methylthiazol-5-yl)ethanone moiety D (C17–C22/N3/O2/S1) are found to be planar with respective root mean square (r.m.s.) deviations of 0.0075, 0.0518, 0.0638 and 0.0179 Å. The dihedral angles A/B, B/C and B/D are 7.52(8)°, 74.36(10)° and 6.85(8)°, respectively. The dihedral angles infer that the moieties A and B are nearly planar to each other and similarly moieties B and D are nearly planar.

In **8** (Fig. 1b and Table 1), the methyl thiazole-4-carboxylate moiety A (C2–C6/N1/O1/O2/S1), 4,5-dihydro-1*H*-pyrazole ring B (C7–C9/N2/N3), bromophenyl ring C (C10–C15/Br1) and chlorophenyl ring D (C16–C21/Cl1) are found to be planar with respective root mean square (r.m.s.) deviations of 0.0579, 0.0082, 0.0183 and 0.0108 Å. The central ring B is twisted at respective dihedral angles of 18.8(2)°, 67.2(1)° and 6.67(3)° with respect to moiety A and rings C and D. The chloro-substituted phenyl ring makes a dihedral angle of 64.5(1)° with respect to

Table 1 Crystal data and structure refinement for compounds **7**, **8** and **10**

Crystal data	**7**	**8**	**10**
CCDC	1981404	1009301	1009302
Chemical formula	$C_{22}H_{20}BrN_3O_2S$	$C_{21}H_{17}BrClN_3O_2S$	$C_{27}H_{22}ClN_5O_3S$
M_r	470.38	490.80	532.00
Crystal system	Triclinic	Triclinic	Orthorhombic
Space group	$P\bar{1}$	$P1$	$Pca2_1$
Temperature (K)	296	296	296
a (Å)	7.3329(4)	4.7441(4)	23.994(4)
b (Å)	11.3359(7)	9.5883(9)	5.0580(9)
c (Å)	13.3196(7)	12.0770(11)	20.359(3)
α (°)	105.658(3)	73.421(5)	90
β (°)	92.689(2)	89.483(5)	90
γ (°)	97.255(3)	86.045(6)	90
V (Å^3)	1053.76(10)	525.23(8)	2470.8(7)
Z	2	1	4
Density	1.482	1.552	1.430
F(000)	480	248	1104
Wavelength (λ)	0.71073 Å	0.71073 Å	0.71073 Å
μ (mm^{-1})	2.073	2.206	0.280
Crystal shape	Needle	Needle	Needle
Crystal colour	Yellow	White	Light yellow
Crystal size (mm)	0.38 × 0.20 × 0.18	0.40 × 0.18 × 0.16	0.42 × 0.22 × 0.16
No. of measured, independent	15 423	8109	20 066
and observed [$I > 2s(I)$] reflections	4064	4306	5563
	2568	3367	2853
R_{int}	0.037	0.027	0.089
Theta range for data collection	2.788 to 26.000	2.222 to 27.502	1.697 to 27.481
Index ranges	$-8 \le h \le 8$	$-5 \le h \le 6$	$-30 \le h \le 31$
	$-13 \le k \le 13$	$-12 \le k \le 12$	$-5 \le k \le 6$
	$-16 \le l \le 16$	$-15 \le l \le 15$	$-26 \le l \le 25$
$(\sin\theta/\lambda)_{max}$ (Å^{-1})	0.617	0.650	
$R[F^2 > 2\sigma(F^2)]$	0.040	0.035	0.047
w$R(F^2)$	0.098	0.077	0.078
S	1.02	1.03	0.92
No. of reflections	4064	4306	5563
No. of parameters	265	263	336
No. of restraints	—	3	1
$\Delta\rho_{max}$, $\Delta\rho_{min}$ (e Å^{-3})	0.43, −0.44	0.17, −0.30	0.23, −0.27

the bromo-substituted ring. This dihedral angle inspection infers that ring B and D are almost parallel. The terminal C atom (C1) is at a distance of 1.3589(7) Å from the plane of moiety A.

In **10** (Fig. 1c and Table 1), the chlorophenyl ring A (C1–C6/Cl1), 4,5-dihydro-1*H*-pyrazole ring B (C7–C9/N1/N2), phenyl ring C (C10–C15), thiazole ring D (C16–C18/N3/S1) and (*E*)-*N*′-(2-hydroxy-3-methoxybenzylidene)formohydrazide group E (C19–C27/N4/N5/O1–O3) are found to be planar with respective r.m.s. deviations of 0.0069, 0.0666, 0.0090, 0.0028 and 0.0156 Å. The thiazole ring D is twisted at a dihedral angle of 8.02(3)° and 1.32(2)° with respect to ring B and group E, respectively. These dihedral angles infer that thiazole ring D and group E are almost parallel. Chlorophenyl ring A makes dihedral angles of 80.04(1)° and 86.7(9)° with respect to ring C and group E, respectively.

Crystal packing and interaction energy analysis

The intermolecular interactions which are responsible for the crystal packing of compounds **7**, **8** and **10** are reported in Table 2 along with the respective interaction energies.

The crystal packing of compound **7** is stabilized by both classical and non-classical noncovalent interactions including C–H···O, C–H···Br, C–H···π and π···π stacking interactions, as shown in Fig. 2. The strong dimer D2 (E_{tot} = −22.3 kcal mol^{-1}) is further stabilized by C–H···π interactions involving the H6 atom from the bromophenyl ring and the Cg4 centroid of the anisole ring [d(H6···Cg4) = 3.83 Å]. In addition, this dimer is stabilized by offset π···π stacking interactions between the centroid of the thiazole ring Cg1 and the centroid of the bromophenyl moiety Cg3, with an inter-centroid separation of 3.8853(2) Å (symmetry: 1 − x, 2 − y, −z) corresponding to a ring offset of 1.573 Å. The contribution of dispersion energy was calculated to be 75.1% towards the stabilization of this structural dimer. The dimer D1 (E_{tot} = −20.6 kcal mol^{-1}) is stabilized by intermolecular C8–H8B···O2 hydrogen bonds involving the O2 atom from the carbonyl group as an acceptor and the H8B atom from the 4,5-dihydro-1*H*-pyrazole ring. The electrostatic and dispersion energies contribute 33.7% and 66.3%, respectively, towards the stabilization of this dimer.

Intermolecular C2–H2···O1 and C8-H8A···O1 hydrogen bonding interactions are responsible for the stabilization of

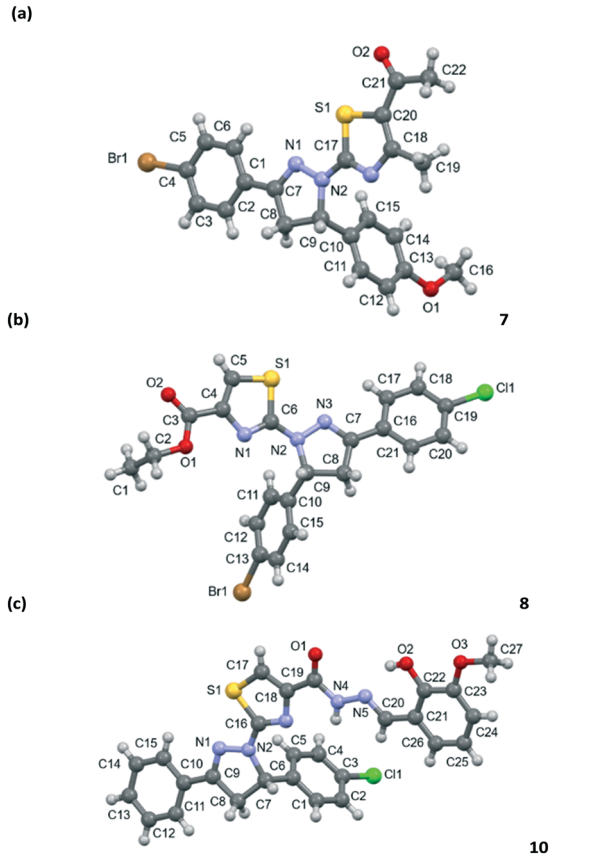

Fig. 1 Molecular structure of compounds **7** (a), **8** (b) and **10** (c). The atom numbering scheme is also given.

dimer D3 (E_{tot} = −12.4 kcal mol^{-1}) with 41.8% electrostatic energy contribution towards the stabilization.

Interestingly, the crystal packing of **7** is further stabilized by (Br1)···π interactions involving the Br1 atom and the centroid Cg4 of the anisole ring [d(Br1···Cg4) = 3.6279(2) Å; <(C4–Br1···Cg4) = 167.80(1)°, symmetry: x, y, −1 + z] and weak C–H···Br hydrogen bonds involving the H19B of the 1-(4-methylthiazol-5-yl)ethanone moiety and the bromine atom of the bromophenyl ring (dimer 4). The intermolecular interaction energy for dimer D4 is −2.9 kcal mol^{-1} and the dispersion energy contributes 84% towards the stabilization of this structural dimer. Further analysis of this dimer is discussed below regarding the physical nature of the Br···π interaction (lone pair···π *vs.* halogen bond).

The energetically weakest dimer D5 (E_{tot} = −2.7 kcal mol^{-1} with 58% contribution of electrostatic energy) is mainly stabilized by C12–H12···O2 hydrogen bonds involving the O2 atom of the 1-(4-methylthiazol-5-yl)ethanone moiety as an acceptor and the H12 atom from the anisole ring.

The crystal packing of **8** shows four molecular dimers and the intermolecular interaction energy of these dimers are between −20.1 and −1.5 kcal mol^{-1}, as shown in Table 2. These dimers are mainly stabilized by C–H···O, C–H···N and C–H···Br hydrogen bonds (Fig. 3). In addition, C–H···π, lone pair (Cl)···π and π···π stacking interactions are responsible for the stabilization of the crystal lattice. The strongest dimer D1 (E_{tot} = −20.1 kcal mol^{-1} with the contribution of 81% dispersion energy) is stabilized by C11–H11···O1 [d(H11···O1) = 2.68 Å] and C11–H11···N1 [d(H11···N1) = 2.83 Å] hydrogen bonds. This structural dimer is also stabilized by π···π stacking interactions involving bromophenyl rings (Cg3) of adjacent molecules with a centroid-to-centroid distance of 4.7441(4) Å (symmetry: 1 + x, y, z) and between the 4,5-dihydro-1*H*-pyrazole ring (Cg2) and the chlorophenyl ring (Cg4), with an inter-centroid distance Cg2···Cg4 of 4.1285(4) Å (symmetry: −1 + x, y, z). Interestingly, (Cl1)···π interactions involving the Cl1 atom and the chlorophenyl ring (Cg4) [d(Cl1···Cg4) = 4.020 Å, <(C19–Cl1···Cg4) = 82.2°] stabilize the dimer D1. The dimer D2 (E_{tot}: −7.3 kcal mol^{-1}) is mainly stabilized by intermolecular C–H···O hydrogen bonds involving the O2 atom of the carbonyl group as an acceptor and the H8B of the 4,5-dihydro-1*H*-pyrazole ring. In addition to the hydrogen bond, this structural motif is also stabilized by C–H···π interactions involving the H5 atom of the thiazole ring and the chlorophenyl ring (Cg4). The electrostatic and dispersion energies contribute 60% and 40%, respectively, towards the stabilization of this dimer. The carbonyl group is also involved as an acceptor for the intermolecular C15–H15···O2 hydrogen bond (dimer D3), with a total interaction energy of −5.7 kcal mol^{-1}. It is important to emphasize that the contribution of electrostatic (58.2%) and dispersion (41.8%) energies are similar. Further, dimer D4 is mainly stabilized by weak C17–H17···Br1 hydrogen bonds and Br1···S1 chalcogen bond. The classification of the Br···S contact has been analyzed by using NBO analysis (see the Theoretical methods section).

The crystal structure of compound **10** is mainly stabilized by intermolecular C–H···N, C–H···O, C–H···π and π···π interactions, as shown in Fig. 4. The most stabilized molecular dimer D1 (E_{tot} = −24.2 kcal mol^{-1}) is formed by C5–H5···N3 and C27–H27A···O2 hydrogen bonds and C–H···π contacts [C27–H27A···Cg5, C20–H20···Cg3 and C8–H8B···Cg4].

In addition, π···π stacking interactions between 4,5-dihydro-1*H*-pyrazole (Cg2) and the phenyl ring (Cg4) are also responsible for the dimer stabilization. The dispersion energy (81%) is contributing more than 4-fold that of electrostatic energy (19%) towards the stabilization. The dimer D2 is generated by intermolecular C–H···O hydrogen bonding interactions involving the H8A of the 4,5-dihydro-1*H*-pyrazole ring and the O3 atom of the methoxy group as an acceptor [d(H8A···O3) = 2.66 Å]. This structural motif is also stabilized by C–H···π contacts involving the H27B atom of the methoxy group and the chlorophenyl ring (Cg3), with H27B···Cg3 distance of 3.03 Å. It is important to emphasize that the contribution of electrostatic energy (60.3%) is higher than that of dispersion energy (39.7%) towards the stabilization of dimer D2.

As shown in Fig. 4, the structural dimer D3 (E_{tot} = −5.6 kcal mol^{-1}) is stabilized by two C11–H11···O1 and C12–H12···O1 hydrogen bonds. The electrostatic and dispersion energies contribute 49.7% and 50.3%, respectively, towards the stabilization of this dimer.

Table 2 Interaction energies (kcal mol^{-1}) of the main intermolecular interactions for various molecular pairs observed in the crystal structure of compounds **7**, **8** and **10**

Dimer	R^a	Symmetry	Involved interactions[b]	Geometry[c] H···A/<(D–H···A)	E_{ele}	E_{pol}	E_{dis}	E_{rep}	E_{tot}
Compound **7**									
D1	6.38	$-x, -y, -z$	C8–H8B···O2	2.53/149	−9.3	−2.4	−23.0	13.8	−20.6
			C19–H19C···Cg3	3.42					
			Cg1···Cg2	4.2636(3)					
D2	3.43	$-x, -y, -z$	C6–H6···Cg4	3.83	−7.2	−2.5	−29.1	15.8	−22.3
			Cg1···Cg3	3.8853(2)					
D3	9.20	$-x, -y, -z$	C2–H2···O1	2.57/174	−5.7	−2.0	−10.7	5.5	-12.4
			C8–H8A···O1	2.67/127					
D4	13.32	x, y, z	Br1···Cg4	3.6279(2)	−0.7	−0.2	−5.1	3.3	−2.9
			C19–H19B···Br1	3.35/146					
D5	11.34	x, y, z	C12–H12···O2	2.54/143	−1.4	−0.9	−1.7	1.0	−2.7
Compound **8**									
D1	4.74	x, y, z	C11–H11···O1	2.68/136	−3.6	−2.4	−25.6	10.2	−20.1
			C11–H11···N1	2.83/160					
			Cg3···Cg3	4.7441(4)					
			Cg2···Cg4	4.1285(4)					
			Cl1···Cg4	4.02					
D2	10.99	x, y, z	C8–H8B···O2	2.51/157	−3.3	−1.2	−6.8	3.5	−7.3
			C5–H5···Cg4	3.50					
D3	9.59	x, y, z	C15–H15···O2	2.75/159	−1.8	−1.1	−6.5	3.3	−5.7
D4	12.08	x, y, z	Br1···S1	3.75	−0.4	0.0	−2.4	1.4	−1.5
			C17–H17···Br1	3.49/126					
Compound **10**									
D1	5.06	x, y, z	C5–H5···N3	2.71/155	−5.1	−3.4	−36.9	20.3	−24.2
			C27–H27A···O2	2.85/130					
			C27–H27A···Cg5	3.51					
			C20–H20···Cg3	3.22					
			C8–H8B···Cg4	2.56					
			Cg2···Cg4	3.71					
D2	12.66	$x + 1/2, -y, z$	C8–H8A···O3	2.66/149	−6.0	−2.0	−5.3	1.8	−10.7
			C27–H27B···Cg3	3.03					
D3	12.04	$x + 1/2, -y, z$	C11–H11···O1	2.68/119	−2.4	−1.3	−3.8	1.5	−5.6
			C12–H12···O1	2.80/114					

[a] R: centroid-to-centroid distance (Å) of the molecular pair (main atomic position). [b] Cg1, Cg2, Cg3, Cg4 and Cg5 are the centroids of the rings S1/C17/N3/C18/C20, N1/N2/C7–C9, C1–C6, C10–C15 and C21–C26, respectively. [c] Geometry of intermolecular contacts (Å, °).

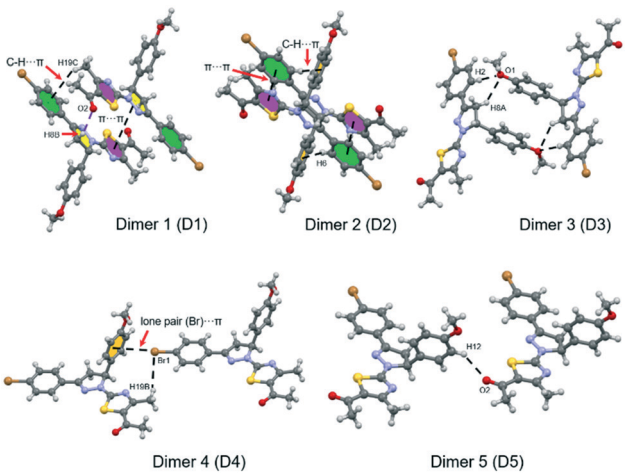

Fig. 2 View of the different dimers observed in the crystal structure of **7**. Intermolecular interactions are shown as dashed lines. Cg1: S1/C17/N3/C18/C20 centroid (violet), Cg2: N1/N2/C7–C9 centroid (yellow), Cg3: C1–C6 centroid (green), Cg4: C10–C15 centroid (orange).

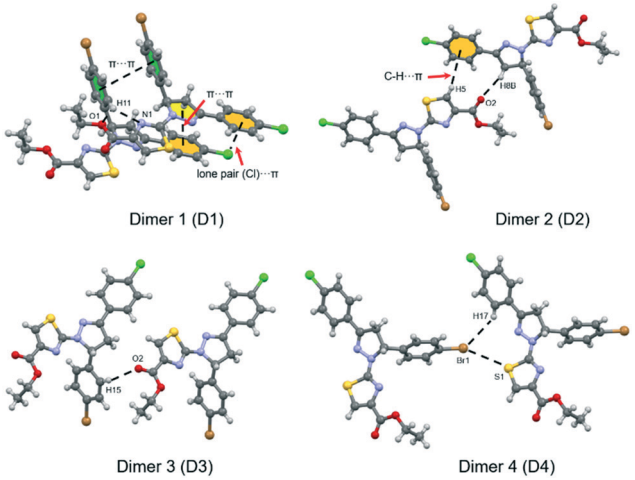

Fig. 3 Partial view of the different structural dimers observed in the crystal structure of **8**. The intermolecular interactions are shown as dashed lines. Cg2: N1/N2/C7–C9 centroid (yellow), Cg3: C1–C6 centroid (green) and Cg4: C10–C15 centroid (orange).

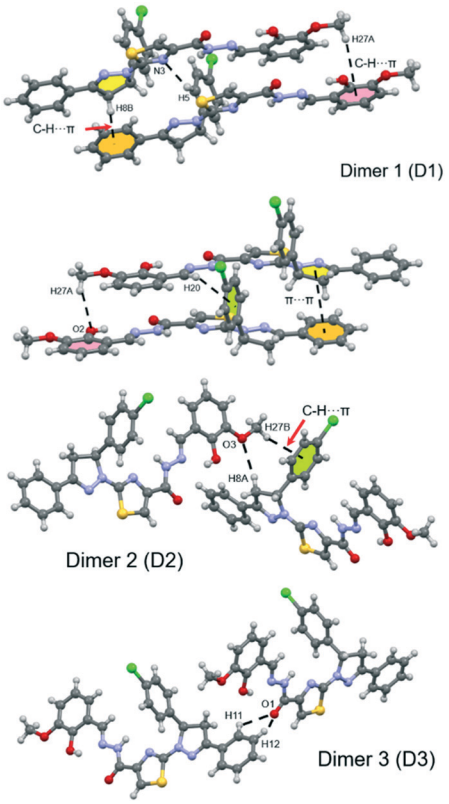

Fig. 4 Partial view of the different structural dimers observed in the crystal structure of **10**. The intermolecular interactions are shown as dashed lines. Cg2: N1/N2/C7–C9 centroid (yellow), Cg3: C1–C6 centroid (green), Cg4: C10–C15 centroid (orange), and Cg5: C21–C26 centroid (pink).

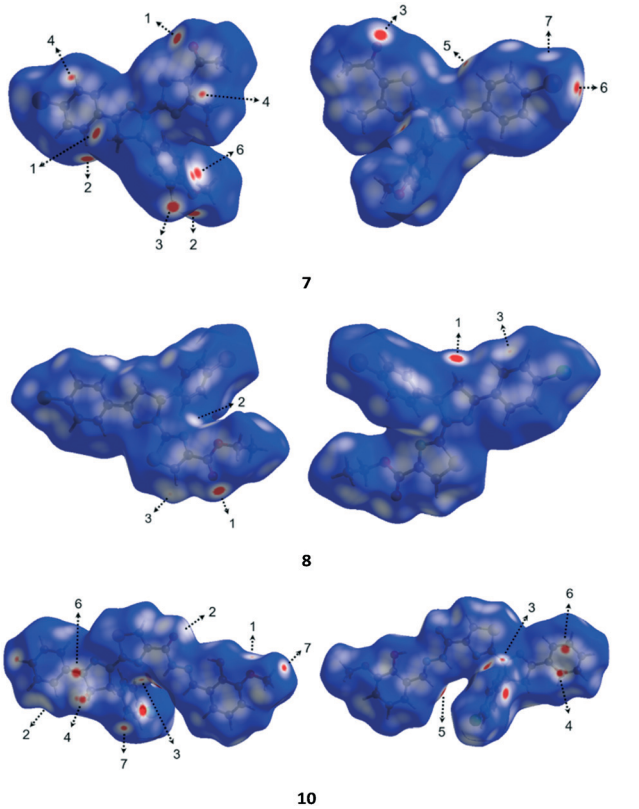

Fig. 5 Hirshfeld surfaces of compounds **7**, **8** and **10** mapped over the d_{norm} function in two orientations (the second molecule is rotated 180° around the horizontal axis of the plot). The labels are discussed in the main text.

Hirshfeld surface analysis

Hirshfeld surface analyses were carried out to understand the nature of packing motifs and the contribution of the main intermolecular interactions which are responsible for the supramolecular architectures in crystalline solids **7**, **8** and **10**. Fig. 5 shows Hirshfeld surfaces mapped over the d_{norm} function, where arrows with numbers indicate close contacts. Graphical plots of the molecular Hirshfeld surfaces mapped over the d_{norm} property use a red-white-blue color scheme, where red indicates shorter contacts, white is used for contacts around the van der Waals (vdW) separation, and blue is used for longer contacts. Full and decomposed two-dimensional fingerprint (FP) plots of the main intermolecular contacts are presented in Fig. 6.

In compound **7**, the largest and red regions labeled 1, 2 and 3 in Fig. 5 are attributed to C8–H8B···O2, C2–H2···O1 and C12–H12···O3 hydrogen bonds, respectively. These contacts are represented as a pair of spikes at $(d_e + d_i) \approx 2.4$ Å in the fingerprint plot (Fig. 6) with a contribution of 12.2% to the total Hirshfeld surface area. Two red spots labeled 4 and 5 (Fig. 5) represent H···C/C···H contacts with a large area fraction of 12.3%.

These contacts are attributed to C19–H19C···Cg3 and C6–H6···Cg4 interactions, which appear in the form of "wings"

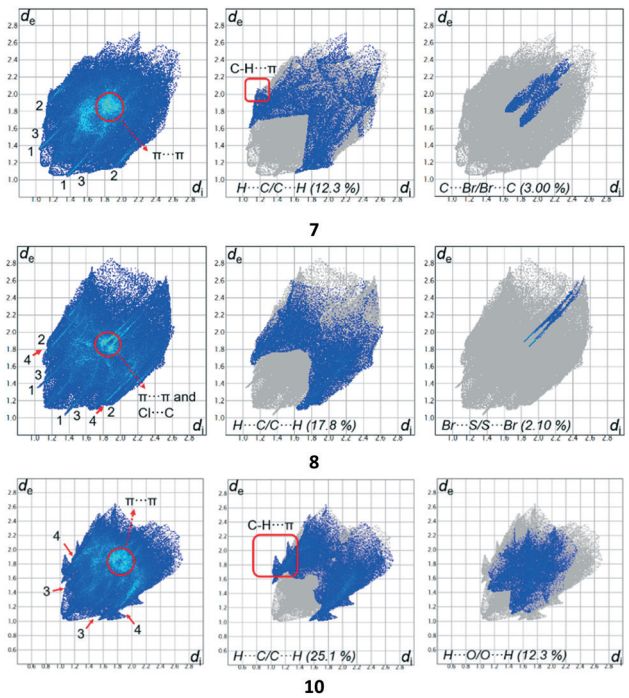

Fig. 6 Full and decomposed two-dimensional fingerprint plots for compounds **7**, **8** and **10**. Close contacts are labeled as follows: (1) H···O/O···H, (2) H···Br/Br···H, (3) H···N/N···H and (4) H···Cl/Cl···H.

on the sides of the fingerprint plots (Fig. 6), characteristic of C–H···π contacts with the shortest value at (d_e + d_i) ≈ 3.2 Å. The red spots labeled 6 in the d_{norm} surface are attributed to lone pair (Br1)···π interactions, as was described previously. These contacts are also visible in the FP plots as two broad spikes at (d_e + d_i) ≈ 3.4 Å with 3.00% contribution to the Hirshfeld surface area. The white spot labeled 7 in the d_{norm} map shows weak H···Br/Br···H contacts attributed to C19-H19B···Br1 hydrogen bonds, which are viewed as broad spikes at (d_e + d_i) ≈ 3.0 Å in the fingerprint plot with a contribution of 9.4% to the Hirshfeld surface area.

In compound **8**, the H···O/O···H contacts labeled 1 in Fig. 5 are attributed to C8–H8B···O2 hydrogen bonds. These contacts appear as sharp spikes in FP with short (d_e + d_i) ≈ 2.3 Å and a contribution of 8.60% to the total Hirshfeld surface. The white spot labeled 2 in the d_{norm} map is attributed to weak C11–H11···N1 hydrogen bonds, which are viewed as a pair of broad spikes at (d_e + d_i) ≈ 2.6 Å in FP with a contribution of 5.4% to the total Hirshfeld surface area.

The occurrence of small red spots (labeled 3) on the Hirshfeld surfaces (Fig. 5) is associated to weak C–H···π contacts involving the H5 atom and the Cg4 centroid with a high contribution of 17.8%. The sharp spikes observed in the decomposed FP plot (Fig. 6) with 2.10% contribution to the total Hirshfeld surface area confirm the relevance of Br···S/S···Br in the supramolecular assembly of compound **8**.

In compound **10**, the small red spots labeled 1 and 2 in the d_{norm} map is attributed to C8-H8A···O3 and C11–H11···O1 hydrogen bonds, respectively. These H···O/O···H contacts are visible in the FP plots as two broad spikes at (d_e + d_i) ≈ 2.5 Å, comprising a 12.3% contribution to the Hirshfeld surface area. The red regions labeled 3 in the d_{norm} surfaces (Fig. 5) are attributed to C5–H5···N3 hydrogen bonds (Fig. 4), and represented as a pair of broad spikes at (d_e + d_i) ≈ 2.5 Å in FP, with a contribution of 4.00%. Like in structure **7**, the small red spots labeled 3, 4 and 5 indicate weak H···C/C···H contacts corresponding to C–H···π interactions (Table 2) which also appear as two types of "wings" in the FP plots with 25.1% contribution to the Hirshfeld surface area. The spots labeled 6 in Fig. 5 are attributed to π···π stacking interactions between Cg2 and Cg4 centroids. The Hirshfeld surface of compound **10** also shows two red spots labeled 7 attributed to vdW H1···H127B interactions.

H···H contacts are also responsible for the crystal packing of the three studied compounds. These interactions are highlighted in the middle of scattered points of FP plots with minimum values of (d_e + d_i) in the range 2.05–2.30 Å and highest contributions of 43.4%, 30.4% and 35.3% to the total Hirshfeld surface area for compounds **7**, **8** and **10**, respectively.

In addition to the hydrogen bonds described previously, the crystal structure of the three compounds are stabilized by π···π stacking interactions, as shown in Table 2. The C···C contacts appear as a distinct pale blue to green area highlighted by a circle at around d_e = d_i = 1.8 Å in the FP plots of the three compounds.

The Hirshfeld surfaces mapped over shape index and curvedness properties (Fig. S1, ESI†) are a very useful tool to identify planar π···π stacking interactions.[39] The pattern of touching red and blue triangles on the shape index surfaces (highlighted as black circles in Fig. S1, ESI†) is characteristic of π···π stacking arrangements[40] and they are visible in the surfaces of all structures. The mentioned interactions are also visible as relatively large and green flat regions delineated by blue circles on the corresponding curvedness surfaces (Fig. S1, ESI†).

DFT calculations

The theoretical study is devoted to analyzing two types of motifs found in the solid state of these compounds, on the one hand, the formation of stacked dimers that present numerous interactions due to the nonaromatic nature of the dihydropyrazolyl ring. On the other hand, we focus on the existence of halogen bonding interactions involving the Br and Cl atoms. In the case of compound **8**, the formation of a Br···S interaction is further analyzed in terms of a competition between halogen (XB) and chalcogen (ChB) bonding.

We have computed the dimerization energies (PBE0-D3/def2-TZVP) and performed the QTAIM and NCIplot index analyses of several dimers of compounds **7**, **8** and **10** retrieved from the X-ray structures. Both computational tools (QTAIM and NCIplot) are very convenient to reveal noncovalent interactions. The existence of a bond path and bond critical point (CP) connecting two atoms is an unambiguous indicator of an interaction. Moreover, the NCIplot analysis gives information regarding the spatial regions between molecules where the interaction is established. Moreover, the color of the isosurface gives valuable information regarding the attractive (blue and green) or repulsive (yellow and red) nature of the interaction.

First of all, we have computed the MEP surfaces of compounds **7**, **8** and **10** in order to investigate the existence of σ-holes in the halogen atoms and the S atom of the thiazole group. The MEP surfaces are shown in Fig. 7 and it can be observed that the MEP maximum is located at the CH_2 group of the 4,5-dihydropyrazolyl ring in compounds **7** and **8** (+28 kcal mol^{-1}) and it is located at the NH bond of the hydrazido group (+34 kcal mol^{-1}) in compound **10**. The MEP minima are located in the O atoms of the keto (**7**), ester (**8**) or hydrazido (**10**) substituents of the thiazole ring. By using a much reduced energy scale, the existence of σ-holes at the halogen atoms is revealed, as highlighted in Fig. 7. The MEP values at the σ-holes range from 6.5 kcal mol^{-1} at Cl of compound **10** to 12 kcal mol^{-1} at Br of compound **7**. The MEP value at the σ-hole of the S atom is significantly more intense (+20 kcal mol^{-1}) than those at the halogen atoms. Moreover, this σ-hole overlaps with the σ-hole of the adjacent H atom (see Fig. 7B, left), and consequently, it is more intense than the σ-hole at the Br atom.

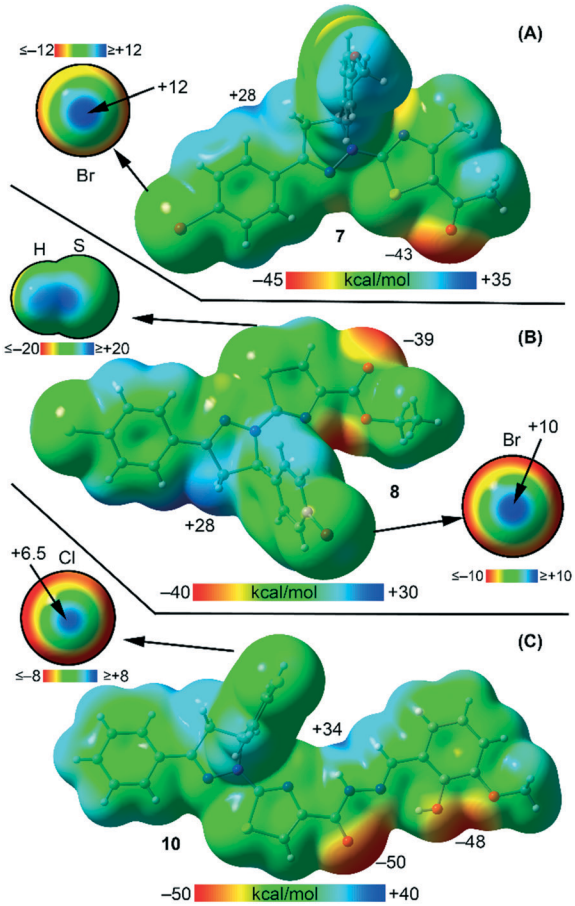

Fig. 7 MEP surfaces (0.001 a.u.) of compounds **7** (A), **8** (B) and **10** (C). The MEP values at selected of the surfaces are indicated in kcal mol^{-1}.

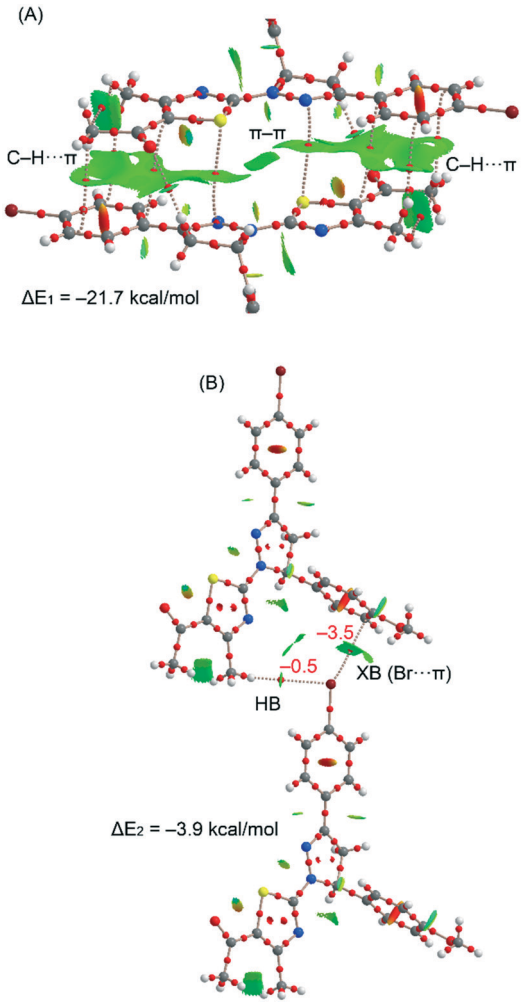

Fig. 8 Combined QTAIM/NCIplot analyses of the stacked dimer (A) and the σ-hole complex (B) for compound **7**. Only bond critical points are represented (as red spheres) for the sake of clarity. For the NCIplot isosurface (0.5 a.u.), the $-0.35 < \mathrm{sign}(\lambda_2)\rho < 0.35$ color scale was used. Gradient cut-off = 0.04 a.u.

Fig. 8 shows the energetic results for the dimers of compound 7 analyzed herein, which consist of the stacked dimer and the halogen bonding complex. The QTAIM analysis of the stacked dimer shows a large number of bond CPs (represented as small red spheres) and bond paths (dashed lines) interconnecting several atoms of both monomers. Moreover, the NCIplot shows extended isosurfaces located between the aromatic, nonaromatic and C–H bonds, thus justifying the large dimerization energy (−21.7 kcal mol^{-1}) and confirming its importance as a strong binding motif in the solid state of **7**. Fig. 8B shows the halogen bonding contact where the electron donor moiety is the electron-rich π-system of the methoxybenzene ring. The XB is characterized by a bond CP and bond path connecting the Br atom to one carbon atom of the ring. Moreover, the presence of a green NCIplot isosurface between the Br atom and the aromatic ring further confirms the existence of the XB interaction (Br···π). The combined QTAIM/NCIplot analysis also reveals the existence of a weak HB between the methyl group and the negative belt of the Br atom. The dimerization energy is very modest (ΔE_2 = −3.9 kcal mol^{-1}), in line with the small MEP value at the σ-hole (see Fig. 8A). In order to investigate the relative importance of both interactions, we have evaluated the individual interaction energies using the QTAIM potential energy density (V_r) predictor measured at the bond CP, as described in the literature (see red numbers in Fig. 8B).[41,42] It can be observed that the XB is stronger than the HB.

The sum of the individual energies computed using the V_r predictor (−4.0 kcal mol^{-1}) is very similar to the dimerization energy (−3.9 kcal mol^{-1}) computed using the supramolecular approach (energy difference between the complex and the sum of the energies of the monomers), thus giving reliability to the QTAIM energy predictor.

Fig. 9 shows the results for compound **8** that are similar to those of compound **7** regarding the interaction energies of the stacked dimer (−21.4 kcal mol^{-1}) and the σ-hole complex (−2.3 kcal mol^{-1}). The combined QTAIM/NCIplot analysis shows that several bond CPs and bond paths interconnect both monomers and extended NCIplot isosurfaces located between the aromatic, nonaromatic and C–H bonds. Fig. 9B shows the halogen/chalcogen bonding contact where it is not

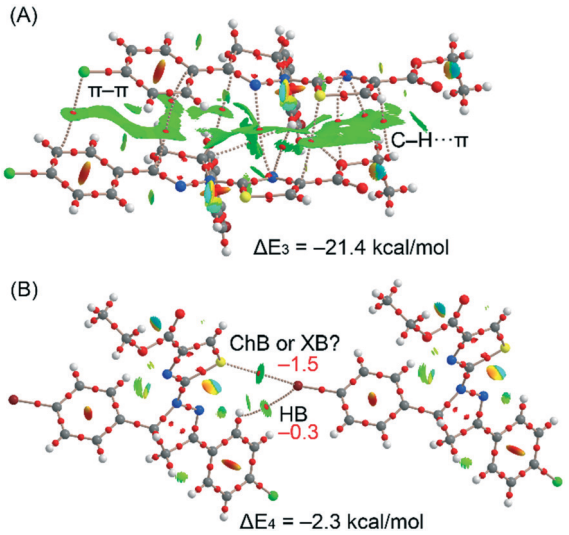

Fig. 9 Combined QTAIM/NCIplot analyses of the stacked dimer (A) and the σ-hole complex (B) for compound **8**. Only bond critical points are represented (as red spheres) for the sake of clarity. For the NCIplot isosurface (0.5 a.u.), the $-0.35 < \text{sign}(\lambda_2)\rho < 0.35$ color scale was used. Gradient cut-off = 0.04 a.u.

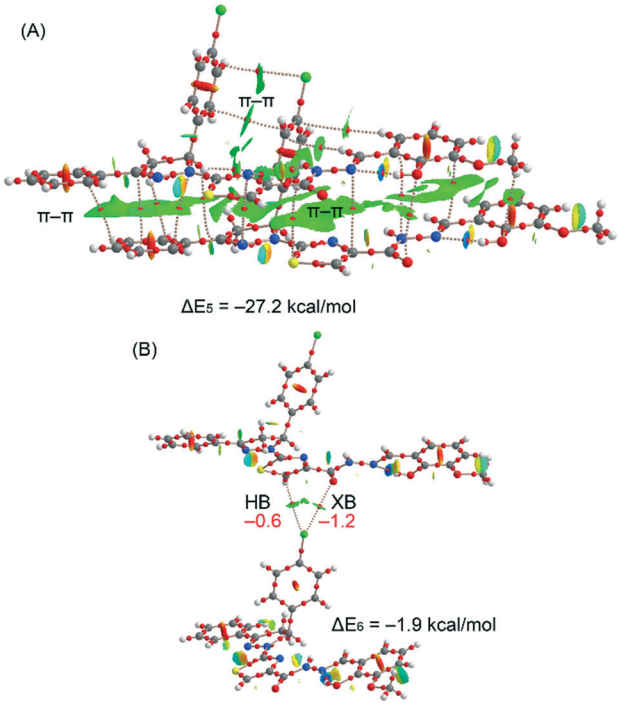

Fig. 10 Combined QTAIM/NCIplot analyses of the stacked dimer (A) and the σ-hole complex (B) for compound **10**. Only bond critical points are represented (as red spheres) for the sake of clarity. For the NCIplot isosurface (0.5 a.u.), the $-0.35 < \text{sign}(\lambda_2)\rho < 0.35$ color scale was used. Gradient cut-off = 0.04 a.u.

evident which atom is acting as an electron donor and which one is the σ-hole donor. This contact is characterized by a bond CP and bond path connecting the Br atom to the S atom of the thiazole ring. Moreover, the presence of a green NCIplot isosurface between both atoms further confirms the existence of an interaction (XB or ChB). The combined QTAIM/NCIplot analysis also reveals the existence of a weak HB between one aromatic H atom and the negative belt of the Br atom. The dimerization energy is very modest (ΔE_4 = −2.3 kcal mol^{-1}) and the evaluation of the individual interaction energies using the V_r predictor demonstrates that the HB is the weakest interaction.

In order to classify the Br···S contact we have performed the natural bond orbital (NBO)[43] analysis, focusing on the second-order perturbation analysis, since it is very convenient to explore donor–acceptor interactions. Remarkably, we have not found any contribution involving the σ*(Br–C) orbital as acceptor, thus ruling out the halogen bond. In contrast, we have found an orbital donor–acceptor interaction from the LP at the Br atom to the antibonding S–C orbital of the thiazole ring, that is Lp(Br) → σ*(S–C) with a concomitant stabilization energy of 0.30 kcal mol^{-1}. Therefore, around 20% of the ChB energy is due to orbital effects.

Finally, a similar study was performed for compound **10** and the results are shown in Fig. 10. Again the stacked dimer presents a very large binding energy due to the large overlap of both molecules, as revealed by the NCIplot. In fact, the interaction energy is stronger than those observed for the dimers of **7** and **8** commented above due to the presence of the additional methoxyphenol ring. However, the halogen bonding complex is weaker than those of **7** and **8**, likely because Cl instead of Br acts as a σ-hole donor, in agreement with the MEP surface analysis. The XB is characterized by a bond CP and bond path interconnecting the Cl and O atoms. Moreover, the QTAIM also shows the existence of an ancillary H-bond where the negative belt of Cl acts as electron donor. This HB is weaker than the XB, as evidenced by the V_r energy predictor.

Concluding remarks

Three new derivatives of 4,5-dihydropyrazolylthiazole have been synthesized and characterized. The supramolecular assemblies observed in their solid-state structures have been analyzed using Hirshfeld surface analysis, DFT calculations and a combination of QTAIM and NCIplot computational tools. All methods suggest that π···π stacking interactions are the most dominant interactions and they have a prominent role in directing the X-ray packing in all complexes. The existence of weak σ-hole halogen bonds has been evidenced in these compounds, and in the case of compound **8**, where an ambiguous Br···S is established, the NBO analysis confirms that the interaction is a chalcogen bond where the Br atom acts as an electron-rich atom [Lp(Br) → σ*(S–C)].

Author contributions

M. M., S. A., S. H., A. M. K., M. A. and M. M. T.: experimental work, investigation and formal analysis. D. M. G.: Hirshfeld surface analysis; visualization; writing – review and editing; funding acquisition. M. N. A. and A. F.: formal analysis;

funding acquisition; methodology; project administration; resources; supervision; validation; visualization; writing – original draft; writing – review and editing.

Conflicts of interest

There are no conflicts to declare.

Acknowledgements

MNA and MM are thankful to The University of Azad Jammu and Kashmir and Quaid-i-Azam University Islamabad Pakistan for financial support. DMG thanks the ANPCyT (PICT 2016-0226) and SCAIT-UNT (Project 683) and AF thanks the MICIU/AEI, grant number CTQ2017-85821-R, FEDER for funding.

Notes and references

1 N. Bakthavatchala Reddy, G. V. Zyryanov, G. Mallikarjuna Reddy, A. Balakrishna, A. Padmaja, V. Padmavathi, C. Suresh Reddy, J. R. Garcia and G. Sravya, *J. Heterocyclic Chem.*, 2019, **56**, 589–596.

2 P. Sharma, K. R. Senwar, M. K. Jeengar, T. S. Reddy, V. Naidu, A. Kamal and N. Shankaraiah, *Eur. J. Med. Chem.*, 2015, **104**, 11–24.

3 V. Kumar, K. Kaur, G. K. Gupta and A. K. Sharma, *Eur. J. Med. Chem.*, 2013, **69**, 735–753.

4 A. Ansari, A. Ali and M. Asif, *New J. Chem.*, 2017, **41**, 16–41.

5 A. M. Isloor, B. Kalluraya and P. Shetty, *Eur. J. Med. Chem.*, 2009, **44**, 3784–3787.

6 A. Isloor, B. Kalluraya, M. Rao and A. Rahiman, *J. Saudi Chem. Soc.*, 2000, **4**, 265–270.

7 D. Sunil and P. Shetty, *Der Pharma Chem.*, 2009, **1**, 19–26.

8 M. Cuenca-Estrella, A. Gomez-Lopez, E. Mellado, G. Garcia-Effron and J. L. Rodriguez-Tudela, *Antimicrob. Agents Chemother.*, 2004, **48**, 3107–3111.

9 R. M. Mohareb, M. Y. Zaki and N. S. Abbas, *Steroids*, 2015, **98**, 80–91.

10 M. Madni, S. Hameed, M. N. Ahmed, M. N. Tahir, N. A. Al-Masoudi and C. Pannecouque, *Med. Chem. Res.*, 2017, **26**, 2653–2665.

11 P. Kumar, N. Chandak, P. Kaushik, C. Sharma, D. Kaushik, K. R. Aneja and P. K. Sharma, *Med. Chem. Res.*, 2012, **21**, 3396–3405.

12 M. Madni, M. N. Ahmed, S. Hameed, S. W. A. Shah, U. Rashid, K. Ayub, M. N. Tahir and T. Mahmood, *J. Mol. Struct.*, 2018, **1168**, 175–186.

13 H. Patel, V. Ugale, A. Ingale and S. Bari, *Lett. Drug Des. Discovery*, 2012, **9**, 840–847.

14 M. Atobe, K. Naganuma, M. Kawanishi, A. Morimoto, K.-i. Kasahara, S. Ohashi, H. Suzuki, T. Hayashi and S. Miyoshi, *Bioorg. Med. Chem. Lett.*, 2013, **23**, 6569–6576.

15 M. Atobe, K. Naganuma, M. Kawanishi, A. Morimoto, K.-i. Kasahara, S. Ohashi, H. Suzuki, T. Hayashi and S. Miyoshi, *Bioorg. Med. Chem. Lett.*, 2013, **23**, 6064–6067.

16 M. N. Ahmed, K. A. Yasin, K. Ayub, T. Mahmood, M. N. Tahir, B. A. Khan, M. Hafeez and M. Ahmed, *J. Mol. Struct.*, 2016, **1106**, 430–439.

17 M. N. Ahmed, K. A. Yasin, S. Hameed, K. Ayub, I.-u. Haq, M. N. Tahir and T. Mahmood, *J. Mol. Struct.*, 2017, **1129**, 50–59.

18 M. N. Ahmed, B. Sadiq, N. A. Al-Masoudi, K. A. Yasin, S. Hameed, T. Mahmood, K. Ayub and M. N. Tahir, *J. Mol. Struct.*, 2018, **1155**, 403–413.

19 B. Wang, M. N. Ahmed, J. Zhang, W. Chen, X. Wang and Y. Hu, *Tetrahedron Lett.*, 2013, **54**, 6097–6100.

20 M. N. Ahmed, K. Ahmad, K. A. Yasin, T. Farooq, B. A. Khan and S. K. Roy, *New J. Chem.*, 2019, **43**, 11316–11333.

21 M. N. Ahmed, M. Arif, F. Jabeen, H. A. Khan, K. A. Yasin, M. N. Tahir, A. Franconetti and A. Frontera, *New J. Chem.*, 2019, **43**, 8122–8131.

22 M. N. Ahmed, K. A. Yasin, S. Aziz, S. U. Khan, M. N. Tahir, D. M. Gil and A. Frontera, *CrystEngComm*, 2020, **22**, 3567–3578.

23 M. Madni, M. N. Ahmed, M. Hafeez, M. Ashfaq, M. N. Tahir, D. M. Gil, B. Galmés, S. Hameed and A. Frontera, *New J. Chem.*, 2020, **44**, 14592–14603.

24 M. Madni, S. Hameed, M. N. Ahmed, K. A. Yasin and M. N. Tahir, *Chin. J. Struct. Chem.*, 2015, **7**, 1013–1018.

25 Y.-M. Lin, Y. Zhou, M. T. Flavin, L.-M. Zhou, W. Nie and F.-C. Chen, *Bioorg. Med. Chem.*, 2002, **10**, 2795–2802.

26 B. F. Abdel-Wahab, H. A. Abdel-Aziz and E. M. Ahmed, *Eur. J. Med. Chem.*, 2009, **44**, 2632–2635.

27 (*a*) J. J. McKinnon, M. A. Spackman and A. S. Mitchell, *Acta Crystallogr., Sect. B: Struct. Sci.*, 2004, **60**, 627–668; (*b*) J. J. McKinnon, D. Jayatilaka and M. A. Spackman, *Chem. Commun.*, 2007, 3814–3816; (*c*) M. A. Spackman and D. Jayatilaka, *CrystEngComm*, 2009, **11**, 19–32; (*d*) M. A. Spackman, *Chem. Rev.*, 1992, **92**, 1769–1797; (*e*) M. A. Spackman, *Phys. Scr.*, 2013, **87**, 048103.

28 M. J. Turner, J. J. McKinnon, S. K. Wolf, D. J. Grimwood, P. R. Spackman, D. Jayatilaka and M. A. Spackman, *CrystalExplorer17*, University of Western, Australia, 2017.

29 C. F. Mackenzie, P. R. Spackman, D. Jayatilaka and M. A. Spackman, *IUCrJ*, 2017, **4**, 575–587.

30 M. J. Frisch, G. W. Trucks, H. B. Schlegel, G. E. Scuseria, M. A. Robb, J. R. Cheeseman, G. Scalmani, V. Barone, G. A. Petersson, H. Nakatsuji, X. Li, M. Caricato, A. V. Marenich, J. Bloino, B. G. Janesko, R. Gomperts, B. Mennucci, H. P. Hratchian, J. V. Ortiz, A. F. Izmaylov, J. L. Sonnenberg, D. Williams-Young, F. Ding, F. Lipparini, F. Egidi, J. Goings, B. Peng, A. Petrone, T. Henderson, D. Ranasinghe, V. G. Zakrzewski, J. Gao, N. Rega, G. Zheng, W. Liang, M. Hada, M. Ehara, K. Toyota, R. Fukuda, J. Hasegawa, M. Ishida, T. Nakajima, Y. Honda, O. Kitao, H. Nakai, T. Vreven, K. Throssell, J. A. Montgomery, Jr., J. E. Peralta, F. Ogliaro, M. J. Bearpark, J. J. Heyd, E. N. Brothers, K. N. Kudin, V. N. Staroverov, T. A. Keith, R. Kobayashi, J. Normand, K. Raghavachari, A. P. Rendell, J. C. Burant, S. S. Iyengar, J. Tomasi, M. Cossi, J. M. Millam, M. Klene, C. Adamo, R. Cammi, J. W. Ochterski, R. L. Martin, K. Morokuma, O. Farkas, J. B. Foresman and D. J. Fox, *Gaussian 16, Revision C.01*, Gaussian, Inc., Wallingford, CT, 2016.

31 C. Adamo and V. Barone, *J. Chem. Phys.*, 1999, **110**, 6158–6169.
32 S. Grimme, J. Antony, S. Ehrlich and H. Krieg, *J. Chem. Phys.*, 2010, **132**, 154104.
33 (*a*) F. Weigend and R. Ahlrichs, *Phys. Chem. Chem. Phys.*, 2005, **7**, 3297–3305; (*b*) F. Weigend, *Phys. Chem. Chem. Phys.*, 2006, **8**, 1057–1065.
34 R. F. W. Bader, *Chem. Rev.*, 1991, **91**, 893–928.
35 J. Contreras-Garcia, E. R. Johnson, S. Keinan, R. Chaudret, J. P. Piquemal, D. N. Beratan and W. Yang, *J. Chem. Theory Comput.*, 2011, **7**, 625–632.
36 E. R. Johnson, S. Keinan, P. Mori-Sanchez, J. Contreras-Garcia, A. J. Cohen and W. Yang, *J. Am. Chem. Soc.*, 2010, **132**, 6498.
37 G. M. Sheldrick, *SADABS, Program for empirical X-ray absorption correction*, Bruker-Nonius, Madison, WI, 1990.
38 G. M. Sheldrick, *Acta Crystallogr., Sect. C: Struct. Chem.*, 2015, **71**, 3–8.
39 A. Di Santo, G. A. Echeverría, O. E. Piro, H. Pérez, A. Ben Altabef and D. M. Gil, *J. Mol. Struct.*, 2017, **1134**, 492–503.
40 M. A. Spackman and D. Jayatilaka, *CrystEngComm*, 2009, **11**, 19–32.
41 E. Espinosa, E. Molins and C. Lecomte, *Chem. Phys. Lett.*, 1998, **285**, 170–173.
42 A. Bauzá and A. Frontera, *ChemPhysChem*, 2020, **21**, 26–31.
43 F. Weinhold, *J. Comput. Chem.*, 2012, **33**, 2363–2379.